JACS
JOURNAL OF THE AMERICAN CHEMICAL SOCIETY
Article
Cite This: J. Am. Chem. Soc. 2018, 140, 1170−1178
pubs.acs.org/JACS

Macrocyclization of Interferon−Poly(α-amino acid) Conjugates Significantly Improves the Tumor Retention, Penetration, and Antitumor Efficacy

Yingqin Hou,[†,⊥] Yu Zhou,[‡,⊥] Hao Wang,[†] Ruijue Wang,[§] Jingsong Yuan,[†] Yali Hu,[†,∥] Kai Sheng,[†] Juan Feng,[‡] Shengtao Yang,[§] and Hua Lu*[,†]

[†]Beijing National Laboratory for Molecular Sciences, Center for Soft Matter Science and Engineering, Key Laboratory of Polymer Chemistry and Physics of Ministry of Education, College of Chemistry and Molecular Engineering, Peking University, Beijing 100871, People's Republic of China

[‡]School of Life Science and Technology, University of Electronic Science and Technology of China, Chengdu 610054, People's Republic of China

[§]College of Chemistry and Environment Protection Engineering, Southwest University for Nationalities, Chengdu 610041, People's Republic of China

[∥]Peking-Tsinghua Center for Life Sciences, Peking University, Beijing 100871, People's Republic of China

Supporting Information

ABSTRACT: Cyclization and polymer conjugation are two commonly used approaches for enhancing the pharmacological properties of protein drugs. However, cyclization of parental proteins often only affords a modest improvement in biochemical or cell-based *in vitro* assays. Moreover, very few studies have included a systematic pharmacological evaluation of cyclized protein-based therapeutics in live animals. On the other hand, polymer-conjugated proteins have longer circulation half-lives but usually show poor tumor penetration and suboptimal pharmacodynamics due to increased steric hindrance. We herein report the generation of a head-to-tail interferon−poly(α-amino acid) macrocycle conjugate *circ*-P(EG_3Glu)$_{20}$-IFN by combining the aforementioned two approaches. We then compared the antitumor pharmacological activity of this macrocycle conjugate against its linear counterparts, *N*-P(EG_3Glu)$_{20}$-IFN, *C*-IFN-P(EG_3Glu)$_{20}$, and *C*-IFN-PEG. Our results found *circ*-P(EG_3Glu)$_{20}$-IFN to show considerably greater stability, binding affinity, and *in vitro* antiproliferative activity toward OVCAR3 cells than the three linear conjugates. More importantly, *circ*-P(EG_3Glu)$_{20}$-IFN exhibited longer circulation half-life, remarkably higher tumor retention, and deeper tumor penetration *in vivo*. As a result, administration of the macrocyclic conjugate could effectively inhibit tumor progression and extend survival in mice bearing established xenograft human OVCAR3 or SKOV3 tumors without causing severe paraneoplastic syndromes. Taken together, our study provided until now the most relevant experimental evidence in strong support of the *in vivo* benefit of macrocyclization of protein−polymer conjugates and for its application in next-generation therapeutics.

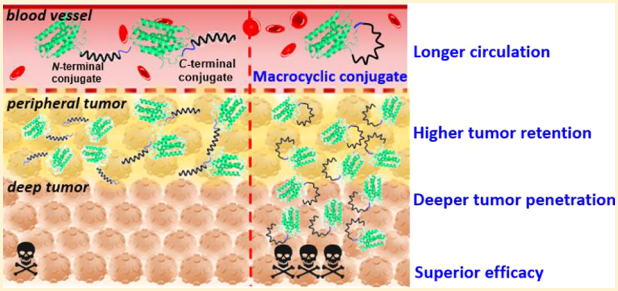

INTRODUCTION

The past two decades have witnessed a rapidly expanding global market for protein-based drugs such as antibodies, cytokines, growth hormones, and genome-editing enzymes against pathologies including infectious diseases, cancers, diabetes, immunodeficiency, and autoimmune diseases.[1] However, the pharmacological activities of protein drugs are often hampered by their intrinsic susceptibility to proteases, poor *in vivo* pharmacokinetics, and strong immunogenicity. To tackle this problem, recently, cyclization of protein has emerged as an appealing approach to create drugs with enhanced protease resistance, thermostability, and binding affinity as a result of their constrained chain conformations.[2] It has also been suggested that macrocyclization of peptides can greatly enhance the permeability due to the smaller size and improved diffusion.[3] However, this strategy has mostly afforded only modest improvement to the parental proteins in biochemical or cell-based *in vitro* assays, and very few studies have systematically evaluated the pharmacological properties of circular protein-based drugs in live animals. Another clinically effective approach relies on the covalent modification of protein with either a synthetic polymer or a genetically fused polypeptide.[4] However, the larger hydrodynamic volume and greater steric hindrance created by the attached polymers would often compromise the pharmacodynamics of the protein drugs.[5] Moreover, similar to many nanoparticle-based medicines,[6]

Received: December 8, 2017
Published: December 20, 2017

DOI: 10.1021/jacs.7b13017
J. Am. Chem. Soc. 2018, 140, 1170−1178

macromolecular drugs are known to have poorer vascular permeability and cannot penetrate into deep solid tumor tissues because of their impeded diffusion across the interstitial space.[7]

We reason that the creation of a head-to-tail protein−polymer macrocycle conjugate, which requires the combination of cyclization and polymer conjugation, could lead to novel protein therapeutics with desired properties conferred by both approaches. Particularly, the constrained conformation of the resultant macrocycle conjugate could further enhance its stability and facilitate its deep penetration across various biological barriers. However, macrocyclization of protein−polymer conjugates remains synthetically challenging with relatively few reports to date. A pioneer work by Ploegh and colleagues showed that cyclized interferon (IFN) overhanging a PEG chain exhibited greater thermostability and circulation half-life over wild-type IFN (wt-IFN).[8] However, the study did not include a comparison between the circular and linear protein−PEG conjugates. In another excellent study, Gao et al. reported the construction of a cyclized GFP attaching a poly(oligo(ethylene glycol) methyl ether methacrylate) (POEGMA), which displayed greater stability and longer tumor retention compared to its linear counterpart.[9] Nevertheless, the conclusion was somewhat weakened by the choice of intratumoral injection with a reporter protein instead of systemic injection with a real therapeutic protein. Moreover, the *in vivo* pharmacodynamics of the conjugates was evaluated in neither study mentioned above. Technically speaking, it is also worth pointing out the two conjugates are tadpole-like topology rather than a head-to-tail macrocycle.

Poly(α-amino acid)s (PαAAs) have been widely considered as promising alternatives to PEG for protein modification because of their excellent biodegradability and modulability.[10] Herein, we report the synthesis and comparative *in vitro* and *in vivo* assessment of *circ*-P(EG_3Glu)$_{20}$-IFN, a head-to-tail macrocyclic IFN-PαAA conjugate, and three structurally similar linear conjugates, *N*-P(EG_3Glu)$_{20}$-IFN, *C*-IFN-P(EG_3Glu)$_{20}$, and *C*-IFN-PEG. Our results find *circ*-P(EG_3Glu)$_{20}$-IFN to show broad and significant improvement in protease resistance, thermostability, circulation half-life, tumor retention and penetration, as well as antitumor efficacy over its linear counterparts. Furthermore, the mice treated with the macrocyclic conjugate are shown to incur significantly prolonged survival rate and less paraneoplastic syndrome. Taken together, our study provides until now the most relevant experimental evidence that strongly supports the various advantages of macrocyclization of *in vivo* and argues for its application in next-generation protein-based therapeutics.

RESULTS AND DISCUSSION

Synthesis of Topological Conjugates. The four conjugates were synthesized by following a previously reported protocol (Figure 1).[11] To enable site-specific conjugation, two IFN mutants were produced, one carrying *N*-cysteine and *C*-LPETGH$_6$ tags (Cys-IFN-LPETG) and another with the *C*-LPETGH$_6$ appendage only (IFN-LPETG). A 20-mer of poly(γ-(2-(2-(2-methoxyethoxy)ethoxy)ethyl-$_L$-glutamate)[12] (P(EG_3Glu)$_{20}$, molecular weight ∼6000 Da) was selected as a model PαAA candidate for IFN modification. The PαAA was tethered to an aminoglycine on one end and a phenyl thioester on the other to generate G_3-P(EG_3Glu)$_{20}$-SPh (Figure S1).[13] Native chemical ligation (NCL)[14] of Cys-IFN-LPETG with G_3-P(EG_3Glu)$_{20}$-SPh afforded the *N*-terminal conjugate *N*-P(EG_3Glu)$_{20}$-IFN

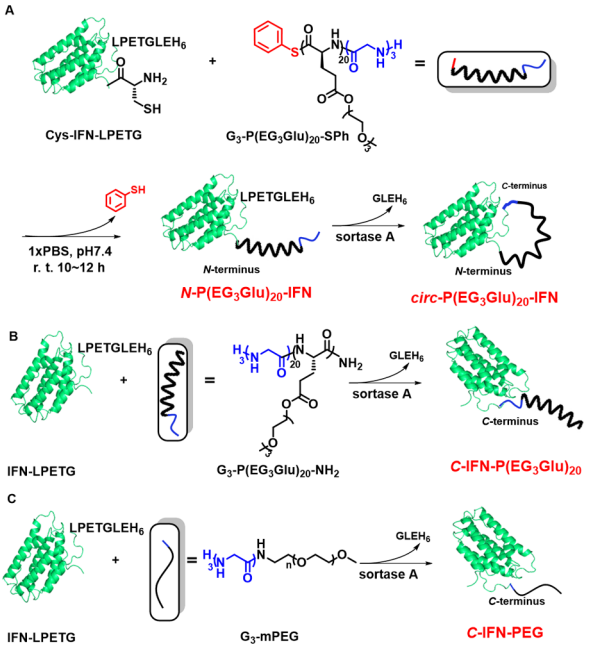

Figure 1. Synthesis of the four IFN-polymer conjugates: the *N*-terminal conjugate *N*-P(EG_3Glu)$_{20}$-IFN and the macrocyclic conjugate *circ*-P(EG_3Glu)$_{20}$-IFN (A), the C-terminal conjugate *C*-IFN-P(EG_3Glu)$_{20}$ (B), and the *C*-terminal PEG conjugate and *C*-IFN-PEG (C).

(Figure 1A). The macrocyclic conjugate *circ*-P(EG_3Glu)$_{20}$-IFN was produced by cyclization of *N*-P(EG_3Glu)$_{20}$-IFN via sortase A mediated ligation (SML)[11,15] (Figure 1A). The *C*-terminal conjugate *C*-IFN-P(EG_3Glu)$_{20}$ (Figure 1B) was synthesized by SML between IFN-LPETG and G_3-P(EG_3Glu)$_{20}$ (Figure S2, P(EG_3Glu)$_{20}$ functionalized with a short aminoglycine tag). For further comparison, a *C*-terminal PEG conjugate *C*-IFN-PEG (Figure 1C) was also produced by the same SML method using IFN-LPETG and G_3-PEG (MW ∼5300 Da, Figure S3) as the conjugation partners.

***In Vitro* Characterization.** All four IFN conjugates showed upper shifted bands on SDS-PAGE gels, thereby indicating

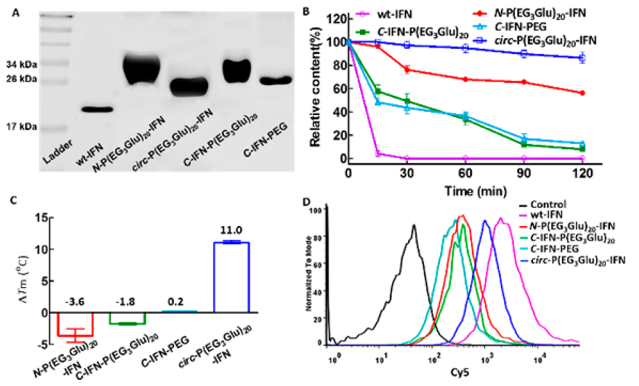

Figure 2. *In vitro* characterization and comparison of wt-IFN, *N*-P(OEG_3-Glu)$_{20}$-IFN, *C*-IFN-P(OEG_3-Glu)$_{20}$, *C*-IFN-PEG, and *circ*-P(OEG_3-Glu)$_{20}$-IFN: (A) SDS-PAGE gel. (B) Protease resistance assay against trypsin degradation. (C) Change of melting temperature (ΔT_m) using thermofluor assay. (D) Flow cytometry analysis of the *in vitro* binding against OVCAR3 cancer cells. Data are expressed as means ± SD in B and C.

successful conjugation (Figures 2A and S4). Notably, *circ*-P(EG_3Glu)$_{20}$-IFN appeared to have slightly higher mobility as

DOI: 10.1021/jacs.7b13017
J. Am. Chem. Soc. 2018, 140, 1170−1178

evidenced by its lower position than the other two IFN-PαAA conjugates in the SDS-PAGE gel, which could be attributed to the constrained conformation after the macrocyclization.[2d] Dynamic light scattering examination of the IFN variants revealed that, when at the single-molecule state, the macrocycle *circ*-P$(EG_3Glu)_{20}$-IFN was slightly and consistently smaller than its three linear analogues (Figure S5). Trypsin digestion indicated that while wt-IFN was rapidly degraded at 37 °C, all conjugates were considerably more stable under the same condition, with *circ*-P$(EG_3Glu)_{20}$-IFN being the most protease-resistant (Figures 2B and S6). Thermofluor assay found *circ*-P$(EG_3Glu)_{20}$-IFN to also be the most thermostable of all, whose melting temperature (T_m) was ∼11 °C above that of wt-IFN (Figures 2C and S7).

To examine the binding affinity of different IFN drugs, we incubated Cy5-labeled wt-IFN or IFN conjugates (Figure S8) with OVCAR-3 and SKOV3 cells, two human ovarian cancer cell lines expressing IFN receptors, at room temperature for 1 h. Flow cytometry analysis showed that *circ*-P$(EG_3Glu)_{20}$-IFN had a greater binding affinity for both types of cells than *N*-P$(EG_3Glu)_{20}$-IFN and *C*-IFN-P$(EG_3Glu)_{20}$ (Figures 2D and S9). To test the *in vitro* antitumor activity,[16] we performed cell viability assay by incubating OVCAR-3 cells with varying concentrations of each IFN conjugate over 72 h. The IC_{50} values of *N*-P$(EG_3Glu)_{20}$-IFN, *C*-IFN-P$(EG_3Glu)_{20}$, *C*-IFN-PEG, and *circ*-P$(EG_3Glu)_{20}$-IFN were determined to be 72, 40, 50, and 21 ng/mL, respectively (Figure S10). Overall, *circ*-P$(EG_3Glu)_{20}$-IFN exhibited the most pronounced therapeutic potential among all four IFN conjugates.

Pharmacokinetics and Biodistribution. To evaluate the *in vivo* pharmacokinetics (PK), we injected each IFN variant intravenously into SD female rats at equal IFN dosage, collected blood samples at various predetermined time points, and subsequently measured the plasma IFN levels by enzyme-linked immunosorbent assay (ELISA). As expected, wt-IFN was rapidly cleared from the plasma and became almost undetectable within 24 h after the injection, whereas the four conjugates all achieved substantially higher plasma IFN concentrations and longer half-lives (*N*-P$(EG_3Glu)_{20}$-IFN: 6.3 h, *C*-IFN-P$(EG_3Glu)_{20}$: 3.5 h, *C*-IFN-PEG: 4.1 h, and *circ*-P$(EG_3Glu)_{20}$-IFN: 8.3 h, compared to wt-IFN: 0.5 h) (Figure 3). Other PK parameters such as the area under the curve (AUC) were summarized in Table S1. It was

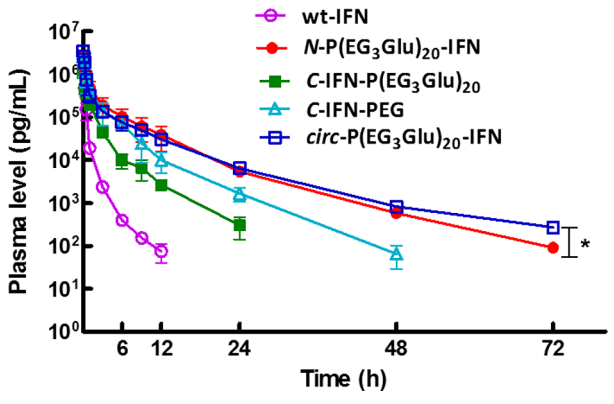

Figure 3. *In vivo* pharmacokinetics of wt-IFN (n = 3), *C*-IFN-PEG (n = 3), *N*-P$(EG_3Glu)_{20}$-IFN (n = 6), *C*-IFN-P$(EG_3Glu)_{20}$ (n = 3), and *circ*-P$(EG_3Glu)_{20}$-IFN (n = 6). Data are expressed as means ± SD; P value was determined by two-way ANOVA analysis: *p < 0.05, **p < 0.01, ***p < 0.001.

postulated that the longest circulation half-life of *circ*-P$(EG_3Glu)_{20}$-IFN was primarily a result of its outstanding protease stability.

For the assessment of biodistribution and intratumoral accumulation, we labeled each IFN variant site-specifically with one molecule of fluorescent dye (e.g., Cy7 or Cy5) (Figure S8). The dye-labeled proteins were intravenously injected into BALB/c-nu female mice bearing subcutaneously inoculated OVCAR-3 tumors. Fluorescence imaging of both the live animals and the dissected organs suggested that wt-IFN was quickly and primarily metabolized by liver and kidney, with kidney being the brightest organ at 48 h (Figure 4B). No apparent drug retention in the tumor areas was observed for wt-IFN *C*-IFN-PEG, whereas both *N*-P$(EG_3Glu)_{20}$-IFN and *C*-IFN-P$(EG_3Glu)_{20}$ showed modest accumulation in the tumor sites before they became undetectable 12 h after injection (Figure 4C). Strikingly, we observed high fluorescence intensity in the tumor following the administration of *circ*-P$(EG_3Glu)_{20}$-IFN (Figure 4C). Even at the end of our study (48 h after the injection), the fluorescence of *circ*-P$(EG_3Glu)_{20}$-IFN was still strong in the tumor site. The enhanced tumor retention of *circ*-P$(EG_3Glu)_{20}$-IFN was further confirmed by ELISA, which showed a 4- to 5-fold enrichment of the macrocyclic conjugate concentration in tumor compared to its three linear counterparts (Figure 4D). When the same study was repeated in BALB/C-nu mice bearing SKOV3 tumors, the intratumoral level of *circ*-P$(EG_3Glu)_{20}$-IFN was, once again, found to be the highest among all IFN variants (Figure S12). We reasoned that the greater enrichment of *circ*-P$(EG_3Glu)_{20}$-IFN in the tumor over the three linear conjugates was due to a combination of multiple parameters including the enhanced stability (Figure 2B,C), the greater binding affinity for the cancer cells (Figure 2D), and the longer half-life (Figure 3). Notably, similar correlations between the circular topology of synthetic polymers and enhanced tumor retention were also reported by Frechet and Szoka.[17]

Deep Tumor Penetration. To investigate the tumor penetration behavior of the IFN drugs, we extracted SKOV3 tumors (∼150 mm^3 in size) from mice and incubated them with Cy5-labeled wt-IFN and various IFN conjugates in serum-free OPTI-MEM medium *ex vivo* at 37 °C for 24 h. The tumors were then sliced, stained with DAPI, and observed with confocal microscopy (Figures 5A and S13). This experiment would thus allow us to solely evaluate the penetration ability of each protein variant without the influence from other parameters such as PK and stability.

As expected, wt-IFN showed the deepest penetration up to 1.5 mm, a result of its smallest size. Interestingly, the penetration depth of *circ*-P$(EG_3Glu)_{20}$-IFN in the tumor reached ∼1.0 mm, whereas the fluorescence of both *N*-P$(EG_3Glu)_{20}$-IFN and *C*-IFN-P$(EG_3Glu)_{20}$ was confined only at the periphery of the tumor with traveled depths less than 0.2 mm. To further examine this penetration effect *in vivo*, we injected each Cy5-labeled IFN variant into SKOV3 tumor-bearing mice via tail vein route. The tumors were then dissected at 24 h, and their cross sections were imaged under a confocal microscope (Figure 5B–D). Unlike the *ex vivo* experiment result, wt-IFN displayed no detectable fluorescent in the tumor, apparently due to its poor PK. Weak fluorescence was detected in the tumors for both *N*-P$(EG_3Glu)_{20}$-IFN and *C*-IFN-P$(EG_3Glu)_{20}$. However, neither conjugate showed uniform distribution as evidenced by an absence of fluorescence in regions with dense malignant tissues. In contrast, we observed intense red fluorescence in tumors from mice administered with *circ*-P$(EG_3Glu)_{20}$-IFN, which was in line with previous tumor retention

DOI: 10.1021/jacs.7b13017
J. Am. Chem. Soc. 2018, 140, 1170–1178

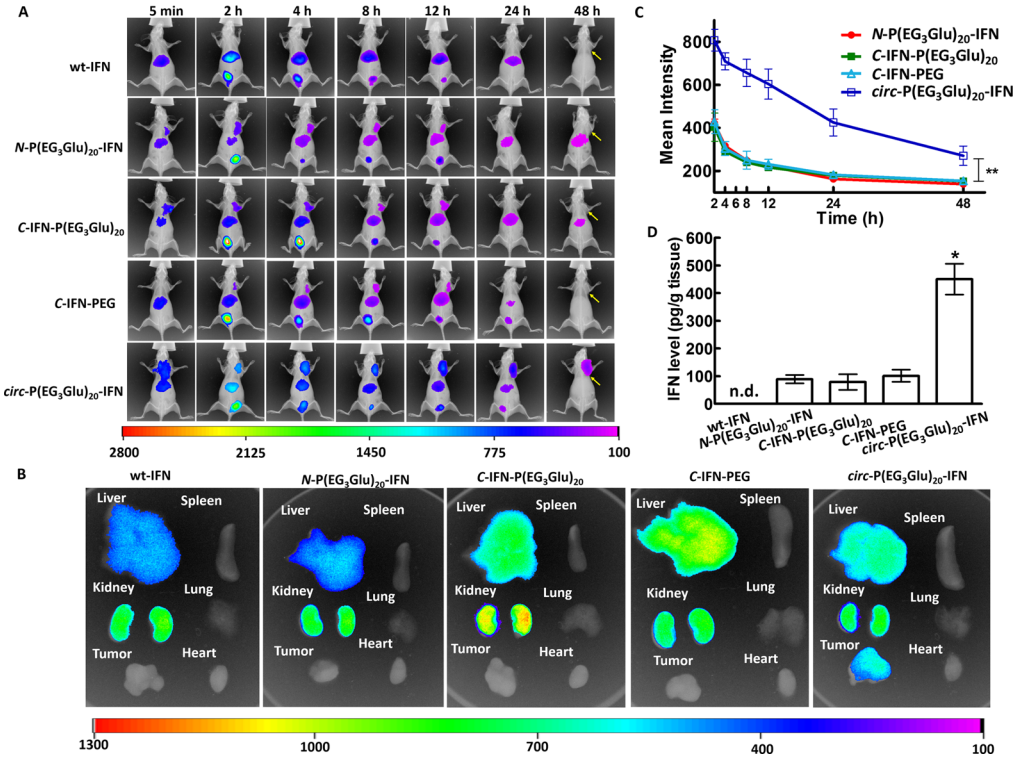

Figure 4. Biodistribution and tumor retention of wt-IFN and IFN conjugates in BALB/C-nu mice bearing OVCAR-3 tumors. (A) Fluorescent images of live animals at different time points. The tumors were inoculated under the right armpit of the mice (indicated by the yellow arrows). (B) Fluorescent images of the extracted organs at 48 h. (C) Time-dependent accumulation of IFN variants in tumor sites based on the Cy7 fluorescence intensity. (D) ELISA quantification of IFN levels in tumors 48 h after the administration. Mice with ~200 mm^3 tumors were infused with various Cy7-labeled wt-IFN or IFN conjugates via tail vein injection at a dose of 1.0 mg IFN/kg body weight. Data are expressed as means ± SD (n = 2); P value was determined by two-way ANOVA analysis: *p < 0.05, **p < 0.01, ***p < 0.001.

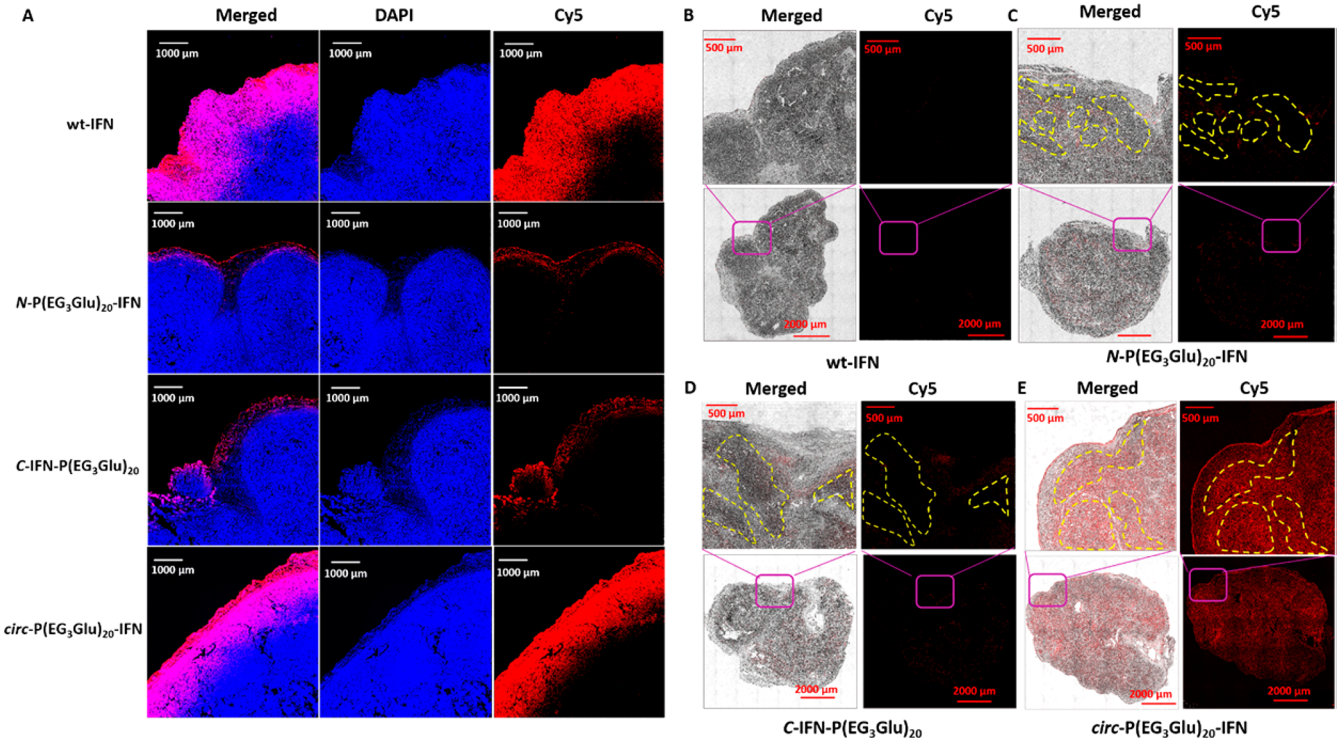

Figure 5. Confocal microscopy of frozen tumor sections to examine the *ex vivo* (A) and *in vivo* (B–D) tumor penetration. For the *ex vivo* study (A), the SKOV3 tumors ~150 mm^3 were cultured with Cy5-labeled wt-IFN or IFN-PαAA conjugates (0.05 mg/mL based on IFN) in Opti-MEM at 37 °C for 24 h; the frozen tumors were sliced and stained with DAPI (blue). For the *in vivo* study (B–D), mice with tumors were infused with Cy5-labeled wt-IFN or various IFN-PαAA conjugates via tail vein injection at a dose of 1.5 mg IFN/kg body weight; the mice were sacrificed and tumors were dissected 24 h after the infusion. The dotted yellow lines indicate the regions of tumor tissues with densely packed malignant cells.

DOI: 10.1021/jacs.7b13017
J. Am. Chem. Soc. 2018, 140, 1170–1178

study (Figure 4). Most remarkably, the fluorescence of the macrocyclic IFN conjugate was homogeneously distributed throughout the entire tumor section, even including areas where the cancer cells were densely packed (Figure 5D). Together, these results strongly supported the notion that macrocyclization would be a feasible strategy to achieve both long circulation and deep tumor penetration, which was highly desirable for treating solid tumors otherwise inaccessible to conventional macromolecule- or nanoparticle-based therapies.

Antitumor Efficacy. We next examined the antitumor efficacy of the conjugates in mice bearing subcutaneous OVCAR-3 xenografts with an average tumor volume of 30 mm^3. On day 0, the mice were divided into six groups with 5−7 animals in each and received intravenous administration of phosphate buffer saline (PBS), wt-IFN, *N*-P$(EG_3Glu)_{20}$-IFN, *C*-IFN-P$(EG_3Glu)_{20}$, *C*-IFN-PEG, or *circ*-P$(EG_3Glu)_{20}$-IFN, respectively, all at a dose of 1.0 mg IFN/kg body weight per infusion. After a total 3−4 injections, on day 21, the average tumor volume in the PBS group rapidly increased to ∼1000 mm^3. In contrast, the administration of the conjugates all significantly suppressed the tumor growth (Figure 6A). Remarkably, *circ*-P$(EG_3Glu)_{20}$-IFN displayed the most pronounced antitumor activity of all, as evidenced by its ability to reduce the average tumor volume to ∼5 mm^3 (Figure 6A). At the end of the study (day 56), 4 out of 6 mice that received the macrocyclic conjugate showed tumor regression to an almost impalpable state. In the survival study, no mice in the PBS, wt-IFN and *C*-IFN-PEG groups remained alive on day 28 due to oversized tumor, significant body weight loss (>15%), and/or other cancer-related complications, whereas those receiving *N*-P$(EG_3Glu)_{20}$-IFN, or *C*-IFN-P$(EG_3Glu)_{20}$ showed considerably extended survival until day 56 (Figures 6B and S14). To our excitement, none of the mice administered with *circ*-P$(EG_3Glu)_{20}$-IFN died within the first 56 days after the initial injection (Figure 6B). Consistent with these findings, K_i-67 staining confirmed the effective inhibition of cancer cell proliferation in mice treated with the macrocyclic conjugate (Figure 6C). Notably, compared with the healthy controls (Figure S15), mice receiving PBS, wt-IFN or *C*-IFN-PEG all developed severe paraneoplastic syndrome on day 28 due to the infiltration of inflammatory immune cells in the liver.[18] In comparison, the symptoms were considerably milder in mice treated with *N*-P$(EG_3Glu)_{20}$-IFN or *C*-IFN-P$(EG_3Glu)_{20}$, and almost non-existent in those administered with *circ*-P$(EG_3Glu)_{20}$-IFN (Figure 6D). To demonstrate *circ*-P$(EG_3Glu)_{20}$-IFN could inhibit established tumor with larger sizes, we modified the regimen by performing the first drug infusion at varying tumor volumes from ∼100 to 300 mm^3. After merely two injections, all mice (n = 7) showed a significant decrease in tumor size on day 14 compared to that on day 0 (>83% reduction, Figure 6E). One week after the third injection, all tumor sizes shrank to 5−10 mm^3 on day 21 (>90% reduction, P value <0.01). Histopathology imaging indicated that none of the IFN conjugates inflicted observable damage to any major organs such as heart, lung, spleen, and kidney (Figure S16). The antitumor efficacy of the conjugates was further assessed in mice bearing xenograft SKOV3 human ovarian cancer cells. Because SKOV3 carcinoma grew more aggressively than OVCAR-3 tumor, the animals were intravenously administered with different IFN drugs at the same dosage as described above (1.0 mg/kg) but at a slightly increased dosing frequency (every 5 days). Again, the treatment with *circ*-P$(EG_3Glu)_{20}$-IFN led to the most pronounced tumor inhibition (n = 10, Figure 6F). No significant loss of body weight was observed in mice receiving any of the IFN conjugates, suggesting that the drugs were all well tolerated at the designated dose in this model (Figure S17).

CONCLUSIONS

In conclusion, our current study provided strong evidence that the attachment of P$(EG_3Glu)_{20}$ to IFN improves the latter's *in vivo* pharmacological performance in a topology-dependent manner. The macrocycle *circ*-P$(EG_3Glu)_{20}$-IFN showed augmented protease resistance, thermostability, binding affinity, and *in vitro* antitumor potency than its linear conjugates *N*-P$(EG_3Glu)_{20}$-IFN, *C*-IFN-P$(EG_3Glu)_{20}$, and *C*-IFN-PEG. Moreover, *circ*-P$(EG_3Glu)_{20}$-IFN exhibited significantly enhanced *in vivo* pharmacokinetic properties, including longer circulation half-life, remarkably higher tumor retention, and increased *ex vivo* and *in vivo* tumor penetration capacity. Because of these advantages, the macrocyclic conjugate demonstrated outstanding *in vivo* antitumor efficacy and safety profile. Taken together, our results thus highlighted for the first time the necessity of integrating both cyclization and polymer conjugation approaches for optimal pharmacological properties, which could provide valuable guidance for the design of next-generation protein-based therapeutics.

EXPERIMENTAL SECTION

Materials. All chemicals were purchased from commercial sources and used as received unless otherwise specified. Phenyl trimethylsilyl sulfide (PhS-TMS) was purchased from Sigma-Aldrich (St. Louis, USA). Anhydrous *N*,*N*-dimethylformamide (DMF) was purchased from Sigma-Aldrich and treated with methyl isocyanate-bounded polystyrene beads (Sigma-Aldrich, St. Louis, USA) prior to polymerization. Cy7-maleimide was synthesized by Okeanos Tech. Co. Ltd. (Beijing, China). γ-(2-(2-(2-Methoxyethoxy)ethoxy)ethyl $_L$-glutamate NCA (EG_3GluNCA), glycine NCA (GlyNCA), wild-type and mutant IFNs, and sortase A 5 M were produced according to established protocols.[11] For *in vivo* studies, endotoxin affinity beads were used to remove endotoxin from all IFN variant. The final concentration of endotoxin was measured by Toxin Sensor Chromogenic LAL Endotoxin Assay Kit (Genscript, Nanjing, China). The results showed that the endotoxin level was less than 0.1 EU/mL, significantly below the safety limit required of medical devices and parenteral drugs (0.5 EU/mL according to FDA of U.S.A.).

Instrumentation. NMR spectra were recorded on a 400 MHz Bruker ARX400 FT-NMR spectrometer. Ultraperformance liquid chromatography−electrospray ionization mass spectrometry (UPLC-ESIMS) analysis was performed on a tandem system equipped with an ACQUITY H-Class UPLC (Waters Corp.) and a quadrupole rods SQ Detector 2 mass spectrometer (Waters Corp.). Separation was performed on a protein BEH C4 column (Waters 300, 1.7 2.150 mm) with ultrapure water (with 0.1% formic acid) and acetonitrile as mobile phase. SDS-PAGE gel and Western blot images were recorded on a typhoon FLA 9500 laser scanner (GE Healthcare Corp.). FPLC separation was performed on an ÄKTA FPLC system (GE Healthcare, Inc.) using a Superdex 200 increase 10/300 GL column. Protein quantitation was conducted by NanoPhotometerP-class (Germany). Thermofluor assay of the protein and conjugates was performed on a Light Cycler 96 Real-time PCR (Roche, Switzerland). Biodistribution of IFN conjugates was imaged by an *in vivo* imaging system (FX Pro, Kodak). Results of cytotoxicity studies were read by an EnSpire Multimode Plate Reader (PerkinElmer, USA). Confocal analysis was performed on a Nikon A1R confocal laser scanning microscope system attached to an inverted ECLIPSE Ti (Nikon Corp., Japan). Flow cytometry analysis was performed on a BD LSR Fortessa equipped with 405, 488, and 640 nm lasers (BD Bioscience. U.S.A.).

Cell Line and Animals. Human ovarian cell line SKOV3 was cultured in 1640 medium (Corning, Manassas, USA) supplemented with 10% FBS, 100 U mL^{-1} of penicillin, and 100 U mL^{-1} of streptomycin. Human ovarian carcinoma OVCAR-3 was grown in 1640

DOI: 10.1021/jacs.7b13017
J. Am. Chem. Soc. 2018, 140, 1170−1178

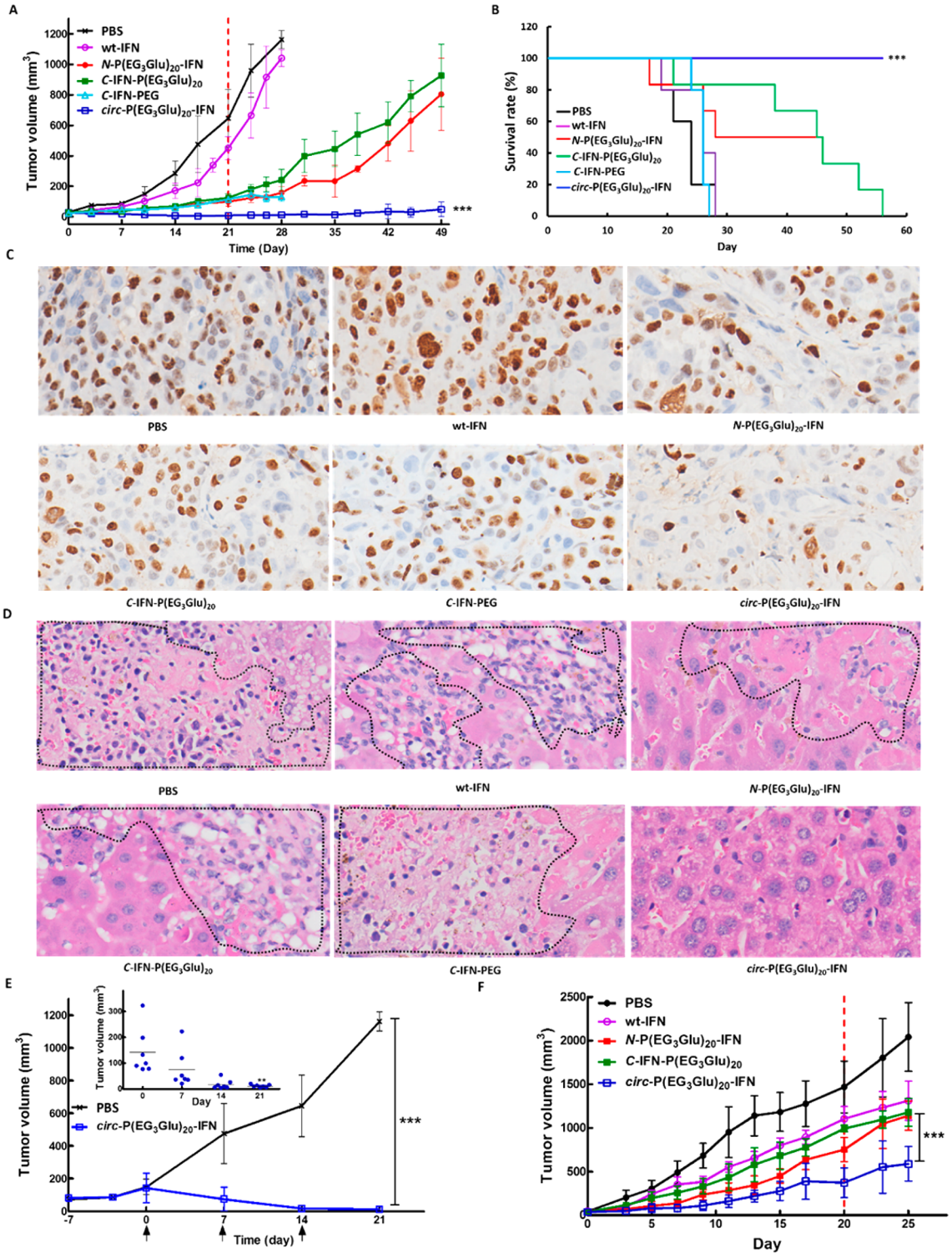

Figure 6. Antitumor efficacy of wt-IFN and IFN conjugates. (A) Tumor growth inhibition curve, (B) survival curve, (C) Ki67-stained tumor sections, and (D) H&E-stained liver sections of OVCAR-3 tumor-bearing mice receiving PBS saline, wt-IFN, *N*-P(EG_3Glu)$_{20}$-IFN, *C*-IFN-P(EG_3Glu)$_{20}$, *C*-IFN-PEG, or *circ*-P(EG_3Glu)$_{20}$-IFN (n = 5−7); BALB/C-nu mice bearing s.c. OVCAR-3 tumor (~30 mm^3) were i.v. injected with PBS saline or IFN-based therapies at 1.0 mg/kg for 3−4 times; therapies started on day 0 and stopped on day 21 (red dashed line in A); black dotted line in (D) circles representative areas of damaged liver by the infiltration of inflammatory immune cells. (E) Tumor growth inhibition curve in BALB/C-nu mice bearing ~100−300 mm^3 OVCAR-3 tumors; mice received PBS or *circ*-P(EG_3Glu)$_{20}$-IFN at 1.0 mg/kg once a week for 3 times; arrows indicate the drug infusion day. Inset: the change of the tumor size of individual mouse in the *circ*-P(EG_3Glu)$_{20}$-IFN group. (F) Growth inhibition curve of BALB/C-nu mice bearing SKOV3 tumors (~40 mm^3) receiving PBS saline, wt-IFN, *N*-P(EG_3Glu)$_{20}$-IFN, *C*-IFN-P(EG_3Glu)$_{20}$, or *circ*-P(EG_3Glu)$_{20}$-IFN (n = 10) at 1.0 mg/kg once every 5 days for 5 times; treatment stopped on day 20 (indicated by red dash line). Data are expressed as means ± SD; *P* value was determined by two-way ANOVA analysis: *p < 0.05, **p < 0.01, ***p < 0.001.

DOI: 10.1021/jacs.7b13017
J. Am. Chem. Soc. 2018, 140, 1170−1178

medium supplemented with 20% FBS, 100 U mL^{-1} of penicillin, 100 U mL^{-1} of streptomycin, and 0.01 mg/mL bovine insulin. Female BALB/c nude mice and female Sprague−Dawley rats were purchased from Vital River Laboratories (Beijing, China). All animal experiments were performed in compliance with the Guideline for the Care and Use of Laboratory Animals and with the approval from the Experimental Animal Ethics Committee in Beijing.

Synthesis of G_3-P(EG_3Glu)$_{20}$-SPh. In a glovebox, EG_3-GluNCA (120 mg, 0.38 mmol, 20 equiv) dissolved in anhydrous DMF (1.2 mL) was mixed with phenyl trimethylsilyl sulfide (PhS-TMS, 3.4 mg, 0.019 mmol, 1.0 equiv). After stirring at room temperature for 4 h, the reaction was poured into ethyl ether (50 mL) to yield a white precipitate. The white solid was collected by centrifugation and dried under vacuum. The residue (∼84 mg) was then redissolved in DMF (2 mL), to which GlyNCA (4.0 mg, 0.040 mmol) in DMF (100 μL) was slowly added. After 3 h, the desired product G_3-P(EG_3-Glu)$_{20}$-SPh was recovered by precipitation in diethyl ether (40 mL), washed with diethyl ether (40 mL × 2), and dried under vacuum. The final product was obtained as a colorless gum-like solid (63 mg, yield 53%) and characterized by ^{1}H NMR. G_3-P(EG_3-Glu)$_{20}$ was synthesized through similar procedures except that hexamethyldisilazane (HMDS)[10e,19] was used as the initiator.

Synthesis of G_3-mPEG. In a glovebox, GlyNCA (12 mg, 0.12 mmol, 3.0 equiv) in anhydrous DMF (200 μL) was slowly added to the solution of mPEG-amine (MW = 5000 Da) in DMF (200 mg in 2.0 mL, 0.04 mmol, 1.0 equiv) and stirred for 4 h at room temperature. DMF was removed under vacuum, and the residue was redissolved in ultrapure water. The product was purified by passing the aqueous solution through a PD-10 size exclusion column.The final product was recovered as a white powder after lyophilization (yield ∼80%).

Synthesis of *N*-P(EG_3Glu)$_{20}$-IFN and *circ*-P(EG_3Glu)$_{20}$-IFN. Cys-IFN-LPETG (5.0 mg, 1.0 equiv) was mixed with G_3-P(EG_3Glu)$_{20}$-SPh (3.0 equiv) in 1× PBS buffer (500 μL, pH 7.4) and incubated at room temperature for 10−12 h. The product *N*-P(EG_3Glu)$_{20}$-IFN was purified on a Superdex 200 increase size exclusion column by FPLC with ∼70% yield. To generate the macrocyclic conjugate *circ*-P(EG_3Glu)$_{20}$-IFN, *N*-P(EG_3Glu)$_{20}$-IFN (0.5 mg, final conc. 50 μM) was mixed with sortase A (0.1 equiv) in Tris-HCl buffer (50 mM, pH 7.5−8.0) supplemented with NaCl (150 mM) and $CaCl_2$ (10 mM). The reaction was incubated at room temperature for 30 min. The crude product was obtained by loading the reaction mixture to a NiNTA column and collecting the flowthrough using a customized washing buffer (20 mM Tris-HCl, 150 mM NaCl, 20 mM imidazole, pH 8.0). Final *circ*-P(EG_3Glu)$_{20}$-IFN was obtained by purifying the crude product on a Superdex 200 increase size exclusion column by FPLC.

Synthesis of *C*-IFN-P(EG_3Glu)$_{20}$ and *C*-IFN-P(EG_3Glu)$_{20}$. IFN-LPETG (1.0 mg/mL, 5.0 mL, 1.0 equiv) was incubated with G_3-P(EG_3-Glu)$_{20}$ (13.7 mg, 10.0 equiv) and sortase A 5 M (0.1 equiv) in Tris-HCl buffer (50 mM, with 10 mM $CaCl_2$, 150 mM NaCl, pH 7.5−8.0) at room temperature for 30 min. The crude product was obtained by loading the reaction mixture onto a NiNTA column and collecting the flowthrough using a customized buffer (20 mM Tris-HCl, 150 mM NaCl, 20 mM imidazole, pH 8.0). The final *C*-IFN-P(EG_3Glu)$_{20}$ was obtained by purifying the crude product on a Superdex 200 increase 10/300 GL column by FPLC with ∼38% yield.

C-IFN-PEG was prepared in a similar protocol with high conversion. The product was purified with a cationic exchange MonoS column, separation yield ∼30%.

General Protocol for Labeling IFN Conjugates with FAM/Cy7/Cy5-Maleimide. For site-specific labeling of IFN, thiol-maleimide chemistry was used. Different dyes were selected and used in different experiments (Cy5 for confocal and flow cytometry analysis, Cy7 for live animal imaging; FAM for trypsin digestion assay). Briefly, the *N*-cys IFN derivative (0.5 mg, 1.0 equiv) was mixed with FAM-maleimide/Cy7/Cy5-maleimide (2.0−3.0 equiv), followed by incubation in Tris-HCl buffer (50 mM, pH 7.4) at room temperature for 40−60 min. The products were purified by repetitive ultrafiltration to remove excessive FAM-maleimide, or by passing through a PD-10 size exclusion column to remove free Cy7/Cy5-maleimide.

Trypsin Digestion Assay. FAM-labeled *N*-P(EG_3Glu)$_{20}$-IFN, *C*-IFN-P(EG_3Glu)$_{20}$, *C*-IFN-PEG, or *circ*-P(EG_3Glu)$_{20}$-IFN (final concentration: 0.22 mg/mL of IFN) in Tris-HCl buffer (50 mM, pH 7.4) was incubated with trypsin (0.01 mg/mL, 0.01 equiv) at 37 °C. At each predetermined time point, an aliquot was sampled, and the reaction was terminated by boiling at 95 °C for 10 min. The samples were then analyzed on the same SDS-PAGE gel. Degradation of the conjugates was evaluated by calculating the relative fluorescent intensity of each band by using a typhoon FLA laser scanner. For the evaluation of wt-IFN degradation, a similar procedure as above was used, with the exception that protein quantitation was based on Coomassie blue staining.

Thermofluor Assay. The thermostability of wt-IFN and the conjugates was assessed by measuring the fluorescence in yellow555 panel (excitation = 533 nm, emission = 572 nm) through Thermofluor assay on a Roche LightCycler96. Briefly, 5 μL of 200× Sypro orange protein gel stain (Thermo) and 45 μL of protein (5−10 μM in 1× PBS buffer) were mixed together and added to a 96-well plate in triplicate. The samples were heated from 37 to 98 °C at a rate of 2.2 °C/min. T_m was calculated by the built-in Roche software.

Flow Cytometry. 5.0 × 10^5 OVCAR-3 or SKOV3 cells were suspended in 50 μL 1× PBS containing 1% BSA, to which was added 0.01 mg/mL Cy5-labeled IFN, *N*-P(EG_3Glu)$_{20}$-IFN, *C*-IFN-P(EG_3Glu)$_{20}$, *C*-IFN-PEG, or *circ*-P(EG_3Glu)$_{20}$-IFN. After incubation at room temperature for 1.0 h, the cells were resuspended in 1× PBS for flow cytometry analysis.

OVCAR-3 Cell Proliferation Inhibition Assay. OVCAR-3 cells were seeded at a density of 5000 per well in a 96-well plate prior to treatment and incubated with IFN variants at gradient concentrations for 72 h (n = 3). The relative cell viability of each group was determined by Cell Titer 96 Nonradioactive Cell Proliferation Assay (Promega, US) by following the manufacturer's protocol. Data were fitted using the GraphPad Prism 5.0 software, and IC_{50} values were expressed as mean ± SD.

Pharmacokinetics. Female Sprague−Dawley rats weighing ∼250 g were used in the pharmacokinetic study. The rats were randomly divided into four groups (n = 3 or 6). The animal subjects in each group were injected through a cannulated jugular vein with one of the following IFN drugs, wt-IFN, *N*-P(EG_3Glu)$_{20}$-IFN, *C*-IFN-P(EG_3Glu)$_{20}$, *C*-IFN-PEG, or *circ*-P(EG_3Glu)$_{20}$-IFN (0.2 mg/kg based on IFN). At selected time points (1, 15, 30 min, 1, 3, 6, 9, 12, 24, 48, and 72 h), blood samples (100 μL each time) were withdrawn from the cannulated jugular vein and allowed to stand at 4 °C for 30 min, followed by centrifugation at 4000*g* for 15 min. The separated plasma was collected and stored at −80 °C before analysis. The concentration of IFN was determined by using a human IFN*α* ELISA Kit (eBioscience). Pharmacokinetic parameters were analyzed by DAS 3.0 software and expressed as mean ± SD.

In Vivo Biodistribution Using OVCAR-3 Model. Six-week-old female BALB/c nude mice were subcutaneously inoculated with 1.0 × 10^7 OVCAR-3 cells suspended in serum-free media mixed with Matrigel (v/v = 1:1, 200 μL). When the tumors grew to ∼250 mm^3 (∼6 weeks), the mice were randomly divided into three groups (n = 2) and injected via the tail vein with one of the following: Cy7-labeled wt-IFN, *N*-P(EG_3Glu)$_{20}$-IFN, *C*-IFN-P(EG_3Glu)$_{20}$, *C*-IFN-PEG, or *circ*-P(EG_3Glu)$_{20}$-IFN at ∼1 nmol (20 μg IFN dosage)/mouse. The mice were anaesthetized with isoflurane and imaged by and *in vivo* imaging system at 5 min, 2, 4, 8, 12, 24, and 48 h. The tumors and the main organs, such as heart, liver, spleen, lung, *in vivo* imaging system. The tumors were weighed, homogenized, and suspended in extraction buffer (10 mM PBS plus 1 mM EDTA, 1% Triton X-100, 0.5% sodium deoxycholate, 1 mM PMSF, phosphatase inhibitor cocktails 2 and 3 (1:100 diluted), and protease inhibitor cocktail (1:100 diluted)). Intratumoral levels of IFN were measured by ELISA as described above.

In Vivo Biodistribution Using SKOV3 Model. Six-week-old female BALB/c nude mice were subcutaneously inoculated with 6.0 × 10^6 SKOV3 cells suspended in 1× PBS (100 μL). When the tumors grew to ∼150 mm^3 (3−4 weeks), the mice were randomly divided into three groups (n = 2) and injected via the tail vein with one of the following, Cy5-labeled wt-IFN, *N*-P(EG_3Glu)$_{20}$-IFN, *C*-IFN-P(EG_3Glu)$_{20}$ or

DOI: 10.1021/jacs.7b13017
J. Am. Chem. Soc. 2018, 140, 1170−1178

circ-P(EG_3Glu)$_{20}$-IFN, at ∼1.5 nmol (30 μg IFN dosage)/mouse. The tumors and the main organs including heart, liver, spleen, lung, and kidney were harvested at 24 h and imaged by an *in vivo* imaging system. The frozen sections of the tumors were analyzed and imaged with confocal microscopy.

Ex Vivo Tumor Penetration Study of IFN and IFN-PαAA Conjugates. SKOV3 tumors ∼150 mm^3 sizes were extracted out and *ex vivo* cultured with Cy5-labeled IFN, *N*-P(EG_3Glu)$_{20}$-IFN, *C*-IFN-P-(EG_3Glu)$_{20}$, or *circ*-P(EG_3Glu)$_{20}$-IFN at 0.05 mg/mL (based on IFN) in Opti-MEM (2.0 mL) at 37 °C for 24 h. The tumors were then washed with PBS (2.0 mL × 3). The frozen sections of the tumors were stained with DAPI, and imaged with confocal microscopy.

In Vivo Antitumor Efficacy. Human OVCAR-3 cells were cultured and implanted into female BALB/c nude mice as described above. The tumors were allowed to grow to ∼30 mm^3 (∼3−4 weeks), and the mice were randomly divided into five groups (n = 5−7 per group, day 0). The animals in each group were then intravenously administered at a dose of 1.0 mg IFN/kg body weight with one of the following, PBS saline, wt-IFN, *N*-P(EG_3Glu)$_{20}$-IFN, *C*-IFN-P(EG_3Glu)$_{20}$, *C*-IFN-PEG, or *circ*-P(EG_3Glu)$_{20}$-IFN. *C*-IFN-P(EG_3Glu)$_{20}$ was injected once every 10 days due to body weight loss, whereas the other reagents were administered weekly. In another study, OVCAR-3 tumors were allowed to grow to ∼100−300 mm^3 before treatments (PBS or *circ*-P(EG_3Glu)$_{20}$-IFN) started at the same dose as described above (a weekly dose of 1.0 mg IFN/kg for three times).

SKOV3 xenograft tumor model was established following a similar procedure as described above. The tumors were allowed to grow up ∼40 mm^3 (2 weeks), and the mice were randomly divided into five groups (n = 10, day 0). The animals in each group were then intravenously administered at a dose of 1.0 mg/kg body weight with PBS saline, wt-IFN, *N*-P(EG_3Glu)$_{20}$-IFN, *C*-IFN-P(EG_3Glu)$_{20}$, or *circ*-P(EG_3Glu)$_{20}$-IFN once every 5 days.

Tumor volume was calculated by the following formula:

$$V = LW^2/2$$

The mice were euthanized if the tumor volume was larger than 1000 mm^3 or the body weight loss was greater than 15%. Statistical analyses were performed using GraphPad Prism software 5.0, and data were expressed as mean ± SD.

Histopathology Evaluation. Histopathology damage was assessed by hematoxylin and eosin (H&E) staining or Ki-67 immunohistochemistry analysis. Briefly, on day 28, one mouse from each group was sacrificed. The tumors and main organs such as liver, kidney, heart, lung, and spleen were collected, embedded with paraffin, and cut into 5-μm-thick sections. The tissues were then stained with H&E or Ki-67 and imaged on a laser scanning quantitative imaging system (Vectra) to assess the histopathology alterations.

■ ASSOCIATED CONTENT

Supporting Information

The Supporting Information is available free of charge on the ACS Publications website at DOI: 10.1021/jacs.7b13017.

^{1}H NMR, Western blot, SDS-PAGE gels, thermal denaturation curves, images of organs, relative body weight of mice, histologic analysis (PDF)

■ AUTHOR INFORMATION

Corresponding Author

*chemhualu@pku.edu.cn

ORCID

Shengtao Yang: 0000-0001-6795-8879

Hua Lu: 0000-0003-2180-3091

Author Contributions

⊥Y. Hou and Y. Zhou contributed equally to this work.

Notes

The authors declare no competing financial interest.

■ ACKNOWLEDGMENTS

This work was financially supported by National Key Research and Development Program of China (2016YFA0201400). We thank the National Natural Science Foundation of China for grants (21722401, 21474004, and 21434008). H.L. thanks the startup funding from Youth Thousand-Talents Program of China.We gratefully thank Prof. Demin Zhou and Prof. Heng Cui for helpful suggestions.

■ REFERENCES

(1) (a) Leader, B.; Baca, Q. J.; Golan, D. E. *Nat. Rev. Drug Discovery* **2008**, *7*, 21−39. (b) Liu, T.; Du, J. J.; Luo, X. Z.; Schultz, P. G.; Wang, F. *Curr. Opin. Chem. Biol.* **2015**, *28*, 66−74. (c) Wang, M.; Zuris, J. A.; Meng, F. T.; Rees, H.; Sun, S.; Deng, P.; Han, Y.; Gao, X.; Pouli, D.; Wu, Q.; Georgakoudi, I.; Liu, D. R.; Xu, Q. B. *Proc. Natl. Acad. Sci. U. S. A.* **2016**, *113*, 2868−2873. (d) Mout, R.; Ray, M.; Tonga, G. Y.; Lee, Y. W.; Tay, T.; Sasaki, K.; Rotello, V. M. *ACS Nano* **2017**, *11*, 2452−2458. (e) Kontos, S.; Hubbell, J. A. *Chem. Soc. Rev.* **2012**, *41*, 2686−2695. (f) Liu, Y.; Du, J. J.; Yan, M.; Lau, M. Y.; Hu, J.; Han, H.; Yang, O. O.; Liang, S.; Wei, W.; Wang, H.; Li, J. M.; Zhu, X. Y.; Shi, L. Q.; Chen, W.; Ji, C.; Lu, Y. F. *Nat. Nanotechnol.* **2013**, *8*, 187−192. (g) Gu, Z.; Biswas, A.; Zhao, M. X.; Tang, Y. *Chem. Soc. Rev.* **2011**, *40*, 3638−3655.

(2) (a) Liu, D.; Wu, W.-H.; Liu, Y.-J.; Wu, X.-L.; Cao, Y.; Song, B.; Li, X.; Zhang, W.-B. *ACS Cent. Sci.* **2017**, *3*, 473−481. (b) Nguyen, G. K. T.; Kam, A.; Loo, S.; Jansson, A. E.; Pan, L. X.; Tam, J. P. *J. Am. Chem. Soc.* **2015**, *137*, 15398−15401. (c) Danial, M.; Tran, C. M. N.; Jolliffe, K. A.; Perrier, S. *J. Am. Chem. Soc.* **2014**, *136*, 8018−8026. (d) Zhang, W.-B.; Sun, F.; Tirrell, D. A.; Arnold, F. H. *J. Am. Chem. Soc.* **2013**, *135*, 13988−13997. (e) Zheng, L. F.; Marcozzi, A.; Gerasimov, J. Y.; Herrmann, A. *Angew. Chem., Int. Ed.* **2014**, *53*, 7599−7603. (f) Camarero, J. A.; Muir, T. W. *J. Am. Chem. Soc.* **1999**, *121*, 5597−5598. (g) Harris, K. S.; Durek, T.; Kaas, Q.; Poth, A. G.; Gilding, E. K.; Conlan, B. F.; Saska, I.; Daly, N. L.; van der Weerden, N. L.; Craik, D. J.; Anderson, M. A. *Nat. Commun.* **2015**, *6*, 10199. (h) Lian, W. L.; Jiang, B. S.; Qian, Z. Q.; Pei, D. H. *J. Am. Chem. Soc.* **2014**, *136*, 9830−9833.

(3) (a) Bock, J. E.; Gavenonis, J.; Kritzer, J. A. *ACS Chem. Biol.* **2013**, *8*, 488−499. (b) Hess, S.; Ovadia, O.; Shalev, D. E.; Senderovich, H.; Qadri, B.; Yehezkel, T.; Salitra, Y.; Sheynis, T.; Jelinek, R.; Gilon, C.; Hoffman, A. *J. Med. Chem.* **2007**, *50*, 6201−6211.

(4) (a) Nguyen, T. H.; Kim, S.-H.; Decker, C. G.; Wong, D. Y.; Loo, J. A.; Maynard, H. D. *Nat. Chem.* **2013**, *5*, 221−227. (b) Fuhrmann, G.; Grotzky, A.; Lukić, R.; Matoori, S.; Luciani, P.; Yu, H.; Zhang, B.; Walde, P.; Schlüter, A. D.; Gauthier, M. A.; Leroux, J.-C. *Nat. Chem.* **2013**, *5*, 582−589. (c) Pokorski, J. K.; Breitenkamp, K.; Liepold, L. O.; Qazi, S.; Finn, M. G. *J. Am. Chem. Soc.* **2011**, *133*, 9242−9245. (d) Klok, H. A. *Macromolecules* **2009**, *42*, 7990−8000. (e) Pelegri-O'Day, E. M.; Lin, E. W.; Maynard, H. D. *J. Am. Chem. Soc.* **2014**, *136*, 14323−14332. (f) Ng, D. Y. W.; Wu, Y. Z.; Kuan, S. L.; Weil, T. *Acc. Chem. Res.* **2014**, *47*, 3471−3480. (g) Wilson, P.; Anastasaki, A.; Owen, M. R.; Kempe, K.; Haddleton, D. M.; Mann, S. K.; Johnston, A. P. R.; Quinn, J. F.; Whittaker, M. R.; Hogg, P. J.; Davis, T. P. *J. Am. Chem. Soc.* **2015**, *137*, 4215−4222. (h) Tao, L.; Mantovani, G.; Lecolley, F.; Haddleton, D. M. *J. Am. Chem. Soc.* **2004**, *126*, 13220−13221. (i) Boyer, C.; Bulmus, V.; Liu, J. Q.; Davis, T. P.; Stenzel, M. H.; Barner-Kowollik, C. *J. Am. Chem. Soc.* **2007**, *129*, 7145−7154. (j) Liu, S. J.; Jiang, S. Y. *Nano Today* **2016**, *11*, 285−291. (k) Luginbuhl, K. M.; Schaal, J. L.; Umstead, B.; Mastria, E. M.; Li, X.; Banskota, S.; Arnold, S.; Feinglos, M.; D'Alessio, D.; Chilkoti, A. *Nat. Biomed. Engin.* **2017**, *1*, 0078. (l) Hu, J.; Wang, G. L.; Liu, X. Y.; Gao, W. P. *Adv. Mater.* **2015**, *27*, 7320−7324. (m) Schellenberger, V.; Wang, C. W.; Geething, N. C.; Spink, B. J.; Campbell, A.; To, W.; Scholle, M. D.; Yin, Y.; Yao, Y.; Bogin, O.; Cleland, J. L.; Silverman, J.; Stemmer, W. P. C. *Nat. Biotechnol.* **2009**, *27*, 1186−1190. (n) Cobo, I.; Li, M.; Sumerlin, B. S.; Perrier, S. *Nat. Mater.* **2015**, *14*, 143−159.

(5) (a) Pasut, G.; Veronese, F. M. *J. Controlled Release* **2012**, *161*, 461−472. (b) Fishburn, C. S. *J. Pharm. Sci.* **2008**, *97*, 4167−4183.

(6) (a) Tang, L.; Yang, X.; Yin, Q.; Cai, K.; Wang, H.; Chaudhury, I.; Yao, C.; Zhou, Q.; Kwon, M.; Hartman, J. A.; Dobrucki, I. T.; Dobrucki, L. W.; Borst, L. B.; Lezmi, S.; Helferich, W. G.; Ferguson, A. L.; Fan, T. M.; Cheng, J. *Proc. Natl. Acad. Sci. U. S. A.* **2014**, *111*, 15344−15349. (b) Liu, Y.; Zhang, D.; Qiao, Z. Y.; Qi, G. B.; Liang, X. J.; Chen, X. G.; Wang, H. *Adv. Mater.* **2015**, *27*, 5034−5042.
(7) Dreher, M. R.; Liu, W. G.; Michelich, C. R.; Dewhirst, M. W.; Yuan, F.; Chilkoti, A. *J. Natl. Cancer Inst.* **2006**, *98*, 335−344.
(8) Popp, M. W.; Dougan, S. K.; Chuang, T. Y.; Spooner, E.; Ploegh, H. L. *Proc. Natl. Acad. Sci. U. S. A.* **2011**, *108*, 3169−3174.
(9) Hu, J.; Zhao, W. G.; Gao, Y.; Sun, M. M.; Wei, Y.; Deng, H. T.; Gao, W. P. *Biomaterials* **2015**, *47*, 13−19.
(10) (a) Knop, K.; Hoogenboom, R.; Fischer, D.; Schubert, U. S. *Angew. Chem., Int. Ed.* **2010**, *49*, 6288−6308. (b) Turabee, M. H.; Thambi, T.; Lym, J. S.; Lee, D. S. *Biomater. Sci.* **2017**, *5*, 837−848. (c) Talelli, M.; Vicent, M. J. *Biomacromolecules* **2014**, *15*, 4168−4177. (d) Lu, Y. J.; Mbong, G. N. N.; Liu, P.; Chan, C.; Cai, Z. L.; Weinrich, D.; Boyle, A. J.; Reilly, R. M.; Winnik, M. A. *Biomacromolecules* **2014**, *15*, 2027−2037. (e) Lu, H.; Wang, J.; Song, Z.; Yin, L.; Zhang, Y.; Tang, H.; Tu, C.; Lin, Y.; Cheng, J. *Chem. Commun.* **2014**, *50*, 139−155.
(11) Hou, Y.; Yuan, J.; Zhou, Y.; Yu, J.; Lu, H. *J. Am. Chem. Soc.* **2016**, *138*, 10995−11000.
(12) Chen, C. Y.; Wang, Z. H.; Li, Z. B. *Biomacromolecules* **2011**, *12*, 2859−2863.
(13) Yuan, J.; Sun, Y.; Wang, J.; Lu, H. *Biomacromolecules* **2016**, *17*, 891−896.
(14) (a) Xia, Y.; Tang, S. C.; Olsen, B. D. *Chem. Commun.* **2013**, *49*, 2566−2568. (b) Bang, D.; Pentelute, B. L.; Kent, S. B. *Angew. Chem., Int. Ed.* **2006**, *45*, 3985−3988. (c) Reinhardt, U.; Lotze, J.; Zernia, S.; Morl, K.; Beck-Sickinger, A. G.; Seitz, O. *Angew. Chem., Int. Ed.* **2014**, *53*, 10237−10241.
(15) Pang, Y.; Liu, J. Y.; Qi, Y. Z.; Li, X. H.; Chilkoti, A. *Angew. Chem., Int. Ed.* **2016**, *55*, 10296−10300.
(16) (a) Montagner, I. M.; Merlo, A.; Carpanese, D.; Pieta, A. D.; Mero, A.; Grigoletto, A.; Loregian, A.; Renier, D.; Campisi, M.; Zanovello, P.; Pasut, G.; Rosato, A. *J. Controlled Release* **2016**, *236*, 79−89. (b) Hu, J.; Wang, G.; Zhao, W.; Gao, W. *J. Controlled Release* **2016**, *237*, 71−77. (c) Bell, S. J.; Fam, C. M.; Chlipala, E. A.; Carlson, S. J.; Lee, J. I.; Rosendahl, M. S.; Doherty, D. H.; Cox, G. N. *Bioconjugate Chem.* **2008**, *19*, 299−305. (d) Dhalluin, C.; Ross, A.; Leuthold, L. A.; Foser, S.; Gsell, B.; Muller, F.; Senn, H. *Bioconjugate Chem.* **2005**, *16*, 504−517. (e) Wang, Y. S.; Youngster, S.; Grace, M.; Bausch, J.; Bordens, R.; Wyss, D. F. *Adv. Drug Delivery Rev.* **2002**, *54*, 547−570. (f) Subramanian, G. M.; Fiscella, M.; Lamouse-Smith, A.; Zeuzem, S.; McHutchison, J. G. *Nat. Biotechnol.* **2007**, *25*, 1411−1419. (g) Yang, J. A.; Park, K.; Jung, H.; Kim, H.; Hong, S. W.; Yoon, S. K.; Hahn, S. K. *Biomaterials* **2011**, *32*, 8722−8729. (h) Zhang, B.; Xu, H.; Chen, J. X.; Zheng, Y. X.; Wu, Y. M.; Si, L. L. L.; Wu, L.; Zhang, C. L.; Xia, G.; Zhang, L. H.; Zhou, D. M. *Acta Biomater.* **2015**, *19*, 100−111.
(17) Chen, B.; Jerger, K.; Frechet, J. M. J.; Szoka, F. C. *J. Controlled Release* **2009**, *140*, 203−209.
(18) Ashour, A. A.; Verschraegen, C. F.; Kudelka, A. P.; Kavanagh, J. J. *J. Clin. Oncol.* **1997**, *15*, 1272−1282.
(19) Lu, H.; Cheng, J. J. *J. Am. Chem. Soc.* **2007**, *129*, 14114−14115.

DOI: 10.1021/jacs.7b13017
J. Am. Chem. Soc. 2018, 140, 1170−1178